# Bound even-parity $J = 0$ and 2 spectra of Ca: A multichannel quantum-defect theory analysis*

J. A. Armstrong, P. Esherick, and J. J. Wynne
*IBM Thomas J. Watson Research Center, Yorktown Heights, New York 10598*
(Received 23 August 1976)

Extensive new data on the even-parity, $J = 0$ and 2 bound states of Ca provide an excellent opportunity for the application of multichannel quantum-defect theory (MQDT) to these spectra. A detailed description of the experimental technique of multiphoton ionization spectroscopy is given, followed by an explicit application of MQDT to the case where interacting Rydberg series go to three distinct limits. MQDT parameter sets are obtained for each of the $^1S_0$, $^1D_2$, and $^3D_2$ series of Ca, permitting quantitative determination of the configuration mixing in each bound state. Several previous assignments of members of the $^1D_2$ series are changed by the analysis. It is found that the quantum defects of the bound energy levels of Ca are determined almost entirely by configuration mixing, with no observable effects of recoupling. This is in contrast to the situation in the rare gases, where angular momentum recoupling has the dominant effect on the quantum defects, with configuration mixing a small additional effect.

## I. INTRODUCTION

The primary aim of this paper is to analyze and interpret the new data obtained[1] by multiphoton ionization spectroscopy on the even-parity $J=0,2$ states of atomic Ca. The tool used in this analysis is the multichannel quantum defect theory (MQDT) due originally to Seaton and coworkers[2] with more recent elaboration by Fano and coworkers.[3]

Within the range of its applicability, MQDT is essentially an exact parametrization of the energy levels and wave functions of interacting Rydberg series. Since it treats each whole series as a unit, it is often superior to conventional analysis based on one-electron configurations supplemented by the use of perturbation theory on a level by level basis. The MQDT is not a perturbation method. Rather it is a theory based on the fact that a highly excited electron sees a Coulomb potential during most of its orbit and hence has an analytically known wave function for that part of the orbit. The wave function is a linear combination of regular and irregular Coulomb wave functions. The theory is parametrized in terms of a small number of physically meaningful quantities, namely, the eigenquantum defects $\mu_\alpha$, and the elements of a unitary transformation matrix $U_{i\alpha}$. The eigendefects are closely related to the eigenvalues of the scattering matrix which describes the electron-electron part of the Hamiltonian. They are also related to the logarithmic derivative of the radial wave function of the system at a certain radius $r_0$. The unitary matrix $U_{i\alpha}$ specifies the transformation which diagonalizes the $S$ matrix for the non-Coulomb part of the scattering of the excited electron by the ion core.

Once the eigendefects and $U$ matrix have been found, it is simple to obtain the mixing coefficients which describe the admixture of an appropriate set of basis functions into the wave function for each bound or autoionizing level observed. The number of such basis functions is small and is equal to the number of interacting channels $M$. This number is often obtainable simply from experimental data presented in a Lu-Fano plot of the quantum defects.[3]

An extensive tabulation of the energy levels of Ca is given by Risberg.[4] An earlier and less accurate tabulation is contained in Moore's tables.[5] The even-parity $4snd\ ^1D_2$ states are listed by Risberg up to $n=7$, and the $^3D_2$ states are given up to $n=11$. The $^3D_2$ series is given to $4s17d$ in a report to be published by P. Camus.[6] The $^1S_0$ series, corresponding mainly to the configurations $4sns$, is listed up to $n=11$ in Ref. 4.

Lu[7] gave Lu-Fano plots for the $^1S_0$ and $^1D_2$ states of Ca using the data available in Ref. 5, but used hand-drawn curves rather than theoretical fits. Lu's two-channel treatment of the $^1S_0$ states continues to apply to the newly measured, high-lying $^1S_0$ states. Reference 5 gave evidence for only three interacting channels in the $^1D_2$ series, whereas we now know that four channels are important. The evidence for the fourth channel comes from the newly measured $^1$high-lying Rydberg states.

The extensive new data obtained by multiphoton ionization spectroscopy have motivated us to analyze the Ca even-parity states in detail using MQDT. However, before presenting the analysis we give a detailed discussion of the experimental technique of multiphoton ionization spectroscopy.

## II. EXPERIMENTAL METHODS

A typical multiphoton ionization spectrum is shown in Fig. 1. The experimental apparatus necessary for obtaining the data presented herein is relatively simple. An oven was used to produce Ca vapor, a pulsed, tunable dye laser was used to excite it, and a simple metal probe was used to detect ions. Accurate calibration of the laser wavelength was obtained by recording, simultaneously with the ionization signal, the absorption of the second harmonic of the laser from the ground state to the well-known odd-parity $^1P_1^o$ states of Ca.[8]

### A. Laser and optical configuration

The experimental configuration is diagrammed in Fig. 2. A Molectron uv-1000 nitrogen laser with a pulse output power of 1 MW was used to pump the dye laser. The laser was operated at the repetition rate of $13\frac{1}{3}$ Hz by synchronizing to every ninth half cycle of the 60-Hz line. This mode of synchronization resulted both in a more stable output power of the nitrogen laser and in reduced noise from 60-Hz pickup by the ionization probe. The 337.1-nm output of the nitrogen-laser pumped dye solutions contained in two magnetically stirred cuvettes, arranged in an oscillator/amplifier configuration.[9] The dye oscillator followed Hänsch's design.[10] A beam expansion of 50 was obtained using a simple planoconcave −4 mm focal length (FL) lens and a 200 mm FL cemented doublet lens. The majority of the newly identified even-parity states of Ca were observed using a dye mixture of equal volumes of a $1.25\times10^{-3}$ $M$ 1, 4-bis (2-methylstyryl) benzene (Pilot Chem.) solution and a saturated solution of diphenyl stilbene (Sigma Chem.), both in $p$-dioxane solvent (Eastman). This wavelength range was scanned using the 13th order of a 316 line/mm echelle grating (PTR Optics No. TF-R2) blazed at 63.6°. The oscillator/amplifier configuration resulted in better transverse mode structure than an oscillator alone; and the linewidth was narrowed from ~0.5 $cm^{-1}$ to ~0.3 $cm^{-1}$. Output powers were typically 50 kW.

The laser wavelength was scanned by turning a micrometer screw against a 3.5-in. lever arm attached to the grating. The wavelength was calibrated by the method to be described below.

### B. Oven and ionization probe

The oven used for obtaining Ca vapor consisted of a 50-cm long pipe with clam-shell heating elements surrounding the central 30 cm. A quartz window was sealed to one end of the pipe via an O-ring and flange. The oven was thermostatically controlled via a chromel-alumel thermocouple placed between the heating elements and the outer wall of the pipe. The temperature, as derived from the thermocouple potential, was typically between 650 and 750 °C, corresponding to Ca vapor pressures between 0.04 and 0.4 Torr. These temperatures should be considered upper bounds, since our observation of the melting point of Ca indicated an inaccuracy of the thermocouple reading. Calcium vapor was kept from depositing on the window by cooling 5 cm of the end of the pipe with circulating water and by the addition of at least 5 Torr of buffer gas.

The ionization signal was detected by an ionization probe inserted into the center of the pipe from the end opposite the window. Two different probe configurations were used in the experiments with Ca. Initially the probe consisted simply of a 2 mm diameter tungsten wire extending axially down the center of a 4 cm inside diameter nickel

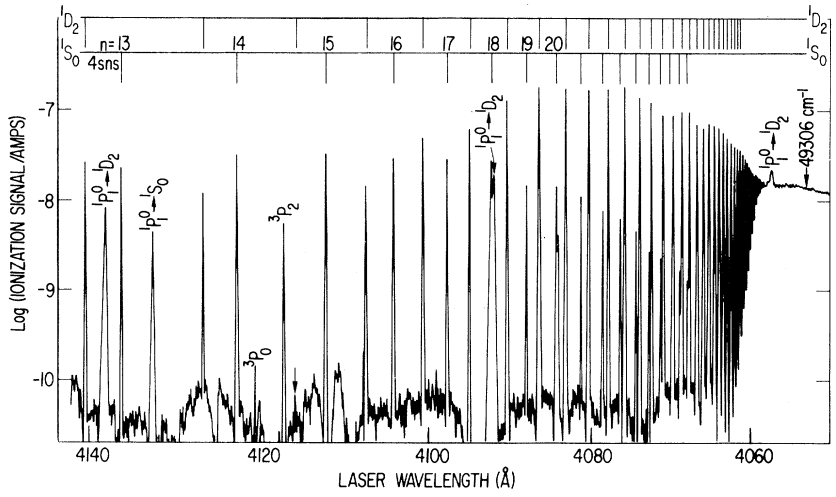


FIG. 1. Multiphoton ionization spectrum of $^1S_0$ and $^1D_2$ states converging on the ionization limit at 49 306 $cm^{-1}$. Experimental conditions: laser polarization, linear; laser intensity, $10^7$ $W/cm^2$; Ca pressure, 0.1 Torr; Kr buffer gas pressure, 10 Torr; voltage on probe, 1 V. Two-photon transitions to $3d^2\,^3P_0$ and $^3P_2$ are also indicated. The lines indicated by $^1P_1^o \rightarrow {}^1S_0$ or $^1P_1^o \rightarrow {}^1D_2$ are transitions from the $4s4p\,^1P_1^o$ level populated by absorption in the wings of the collision-broadened line profile.

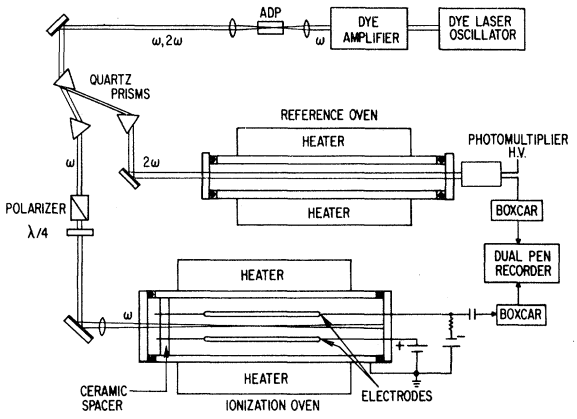


FIG. 2. Experimental configuration.

pipe. Although this served as an excellent ion detector, the electric field near the probe was not uniform. Since this left an uncertainty in the magnitude of the applied field, a parallel plate configuration was later adopted for the ionization probe. In this case two 15-cm long stainless-steel plates were held parallel to one another in the center of a 5-cm inside diameter stainless-steel pipe via 2-mm stainless rod extensions supported by ceramic spacers placed outside of the hot zone. The 1-cm wide, 0.2-cm thick plates were separated by 0.5 cm. Signals were detected by coupling an oscilloscope and/or a Keithley 881 boxcar integrator to one of the probes through a 0.01 uf capacitor. This blocking capacitor allowed the application of dc bias potentials to the both electrodes.

Typical ionization signal pulses observed on the oscilloscope with the parallel plate probe are shown in Fig. 3. Note the compression of the signal in time as the applied field is increased or as the laser beam is moved closer to the collecting electrode. The ion collection efficiency was observed to decrease whenever the potential difference between the two plates was less than 0.5 V or greater than ~10 V. This was true for signals from the continuum above the first ionization limit (49 306 $cm^{-1}$) as well as for signals from bound-state resonances. If the voltage was increased above ~10 V (depending on buffer gas pressure and temperature), a glow discharge could be seen between the plates. Applied fields greater than ~10 V/cm also led to measurable Stark shifts and to mixing of the high-lying Rydberg states. This will be discussed below.

### C. Wavelength calibration and determination of $J$

It is experimentally simple to distinguish between $J=0$ and $J=2$ states when, as in Ca, the initial state has $J=0$. In this case, two photon excitation with a circularly polarized laser beam occurs

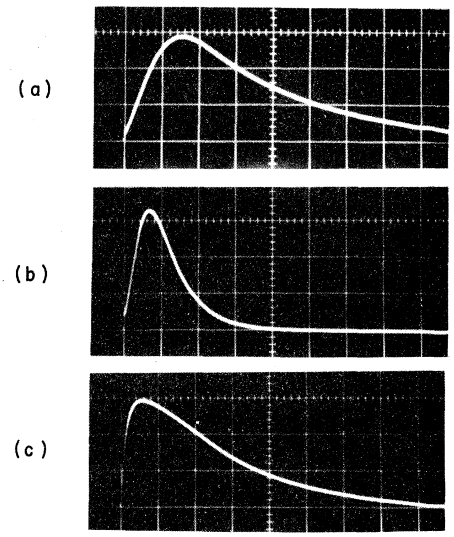


FIG. 3. Typical ionization pulses obtained with parallel plate electrodes and a 100 kΩ load resistor. Vertical: 10 mV/div; horizontal: 0.1 msec/div. (a) Voltage between plates, $V=0.4$ V, beam focused midway between the plates; (b) $V=3.78$ V, beam focused as in (a); (c) $V=0.4$ V, beam focused closer to collecting (negative) electrode.

to final states with $|m|=2$, ruling out all $J=0$ states. Experimentally, the laser was first linearly polarized with a Glan-Taylor prism, and then directed through a quarter-wave plate. Rotation of the retardation plate switched the laser polarization between linear and circular. To determine quickly which peaks were strongly affected, a Fresnel rhomb was used for scans over wide wavelength regions. For more accurate measurements of polarization ratios, a Soleil-Babinet compensator was used. Such measurements showed the signals from $^1S_0$ states to be reduced by a factor 300 in circularly (as compared to linearly) polarized light, whereas the $^1D_2$ states increased in intensity by a factor 1.5, as predicted by angular momentum selection rules.[11]

To obtain accurate energies, $E$, and quantum defects for the newly observed states, we calibrated the laser wavelength for each spectrum scanned. The uncertainty in the effective quantum number $n^*$ increases with $n^*$ according to $\Delta n^* = n^{*3}\Delta(E - I_s)/2R$. Thus accurate wavelength measurement becomes more critical to the calculation of $n^*$ as one nears the ionization limit $I_s$. An ideal wavelength calibration would minimize these errors by providing a high density of points in this critical region. Such a calibration source is readily available in the form of the well-known $4snp\ ^1P_1^o$ Rydberg series, which converges on the same ionization limit as the newly observed even-parity states. The absorption wavelengths of this series have re-

cently been measured[8] with an accuracy of $10^{-4}$ nm. These known one-photon absorption wavelengths were used to calibrate the tunable laser as follows.

The dye laser was frequency doubled by focusing it with a 15-cm FL lens into an ammonium dihydrogen phosphate (ADP) crystal cut and polished perpendicular to the 110 direction. The laser, polarized along $\bar{1}10$, propagated along the 110 direction generating second harmonic polarized along 001. The 15-mm long ADP crystal was orders of magnitude longer than the coherence length at 415 nm. Although phase matching at these wavelengths could not be accomplished, second-harmonic intensity was sufficient to produce 100 mV signals when detected by an EMI G26G315 phototube (Rb-Te photocathode) operating with a gain of about 1000. After recollimation with a 15-cm FL quartz achromat, the fundamental and second harmonic were separated using a quartz prism. The particular arrangement of prisms shown in Fig. 2 was used in order to minimize beam wander due to the prism dispersion over the scanned wavelengths. Transmission of the second-harmonic beam through a second oven containing Ca was then monitored in order to record the $^1P_1^o$ absorption series. This reference oven consisted of a stainless-steel pipe heated over a 50-cm region, with uv-grade quartz windows $o$-ring sealed on the ends. The absorption signal was recorded on the same chart as the ionization signal. The signals were detected by matched boxcar integrators with identical time constants to minimize systematic errors. Since the absorption wavelengths of the $4snp\ ^1P_1^o$ series have been measured up to $n=79$, each spectral scan could include as many as 50 well-defined calibration wavelengths.

The explicit calibration procedure used was to measure the positions of the $^1P_1^o$ state absorptions on a chart and to fit these measurements via standard least-squares fitting techniques[12] to a function expected to describe reasonably accurately the characteristics of the wavelength drive. In most cases this function was a second-order polynomial plus a sinusoidal term with period equivalent to one rotation of the micrometer screw. The precision of a particular scan was given by the average rms deviations from the known wavelengths.[8] Wavelengths for resonances observed in the ionization signal were obtained by applying this calibration function to the measured positions of these peaks on the chart. By averaging the results of some ten scans, the relative errors were reduced for most of the newly observed peaks to less than 0.1 $cm^{-1}$. The energies of the observed even-parity states arrived at using this procedure are presented in Tables I and II. These data are subject to systematic error (of the order of 0.05 $cm^{-1}$) from two sources described below.

Stark shifts and mixing of the high-lying Rydberg states were observed at applied fields greater than ~10 V/cm. With an applied field of 25 V/cm, $^1D_2$ states near $n^*=30$ shifted by $-0.3$ $cm^{-1}$. At these fields two new series of weak peaks appeared in the spectrum for $n^*>20$. One series coincided with the $^1P_1^o$ states being observed simultaneously via single-photon absorption in the reference oven. We have tentatively identified the other series as $^1F_3^o$, although this series has not yet been identi-

TABLE I. Observed and calculated[a] term values for $^1S_0$ states of calcium.

| Approximate configuration | Experimental ($cm^{-1}$) | Calculated ($cm^{-1}$)[a] |
|---|---|---|
| $4s4s$ | 0.00 | ... |
| $4s5s$ | 33 317.26 ± 0.10[c] | 33 414.01[b] |
| $4s6s$ | 40 690.44 ± 0.10[c] | 40 690.44 |
| $4p^2$ | 41 786.28 ± 0.10[c] | 41 786.27 |
| $4s7s$ | 44 276.54 ± 0.10[c] | 44 276.62 |
| $4s8s$ | 45 887.20 ± 0.10[c] | 45 886.95 |
| $4s9s$ | 46 835.05 ± 0.10[c] | 46 835.02 |
| $4s10s$ | 47 437.47 ± 0.10[c] | 47 437.59 |
| $4s11s$ | 47 843.76 ± 0.10[c] | 47 843.97 |
| $4s12s$ | 48 131.21 ± 0.64 | 48 130.88 |
| $4s13s$ | 48 341.17 ± 0.64 | 48 340.94 |
| $4s14s$ | 48 499.44 ± 0.23 | 48 499.33 |
| $4s15s$ | 48 621.44 ± 0.10 | 48 621.70 |
| $4s16s$ | 48 718.10 ± 0.10 | 48 718.20 |
| $4s17s$ | 48 795.50 ± 0.10 | 48 795.64 |
| $4s18s$ | 48 858.72 ± 0.11 | 48 858.72 |
| $4s19s$ | 48 910.74 ± 0.08 | 48 910.79 |
| $4s20s$ | 48 954.43 ± 0.08 | 48 954.27 |
| $4s21s$ | 48 990.88 ± 0.08 | 48 990.95 |
| $4s22s$ | 49 022.13 ± 0.08 | 49 022.18 |
| $4s23s$ | 49 048.99 ± 0.08 | 49 048.99 |
| $4s24s$ | 49 072.16 ± 0.08 | 49 072.17 |
| $4s25s$ | 49 092.42 ± 0.05 | 49 092.35 |
| $4s26s$ | 49 110.05 ± 0.05 | 49 110.02 |
| $4s27s$ | 49 125.64 ± 0.05 | 49 125.59 |
| $4s28s$ | 49 139.40 ± 0.05 | 49 139.38 |
| $4s29s$ | 49 151.59 ± 0.05 | 49 151.64 |
| $4s30s$ | 49 162.47 ± 0.07 | 49 162.60 |
| $4s31s$ | 49 172.43 ± 0.08 | 49 172.43 |
| $4s32s$ | 49 181.49 ± 0.17 | 49 181.28 |
| $4s33s$ | | 49 189.28 |
| $4s34s$ | | 49 196.54 |
| $4s35s$ | | 49 203.14 |
| $4s36s$ | | 49 209.16 |
| $4s37s$ | | 49 214.66 |
| $4s38s$ | | 49 219.71 |
| $4s39s$ | | 49 224.35 |
| $4s40s$ | | 49 228.63 |

[a] MQDT calculated term values using parameters of Table III(b).

[b] This state not included in least-squares fit.

[c] Term values from Ref. 4. Errors listed were used to weight the least-squares fit, and do not necessarily reflect the actual accuracy of this data.

TABLE II. Observed and calculated[a] term values for $^1D_2$ states of calcium.

| Approximate configuration | Experimental ($cm^{-1}$) | Calculated ($cm^{-1}$)[a] | Approximate configuration | Experimental ($cm^{-1}$) | Calculated ($cm^{-1}$)[a] |
|---|---|---|---|---|---|
| $4s3d$ | 21 849.61 | (b) | $4s\,41d$ | 49 236.58 ± 0.05 | 49 236.58 |
| $4s4d$ | 37 298.31 ± 1.0[c] | 37 298.31 | $4s42d$ | 49 239.93 ± 0.05 | 49 239.93 |
| $4p^2$ | 40 719.87 ± 1.0[c] | 40 719.86 | $4s43d$ | 49 243.05 ± 0.05 | 49 243.05 |
| $4s5d$ | 42 919.07 ± 1.0[c] | 42 919.17 | $4s44d$ | 49 245.95 ± 0.05 | 49 245.95 |
| $4s6d$ | 44 989.88 ± 1.0[c] | 44 989.17 | $4s45d$ | 49 248.67 ± 0.05 | 49 248.66 |
| $4s7d$ | 46 199.23 ± 0.56[d] | 46 199.73 | $4s46d$ | 49 251.22 ± 0.05 | 49 251.19 |
| $4s8d$ | 46 948.98 ± 0.56 | 46 948.37 | $4s47d$ | 49 253.56 ± 0.05 | 49 253.55 |
| $3d5s$ | 47 449.36 ± 0.63[e] | 47 450.26 | $4s48d$ | 49 255.76 ± 0.05 | 49 255.77 |
| $4s9d$[f] | 47 812.57 ± 0.63 | 47 811.76 | $4s49d$ | 49 257.81 ± 0.05 | 49 257.85 |
| $4s10d$ | 48 083.42 ± 0.63[g] | 48 083.22 | $4s50d$ | 49 259.76 ± 0.05 | 49 259.80 |
| $4s11d$ | 48 291.01 ± 0.63 | 48 290.89 | $4s51d$ | 49 261.62 ± 0.05 | 49 261.63 |
| $4s12d$ | 48 451.73 ± 0.10 | 48 451.82 | $4s52d$ | 49 263.30 ± 0.05 | 49 263.36 |
| $4s13d$ | 48 578.40 ± 0.13 | 48 578.24 | $4s53d$ | 49 264.91 ± 0.05 | 49 264.99 |
| $4s14d$ | 48 679.02 ± 0.10 | 48 678.99 | $4s54d$ | 49 266.47 ± 0.06 | 49 266.53 |
| $4s15d$ | 48 760.31 ± 0.10 | 48 760.43 | $4s55d$ | 49 268.06 ± 0.08 | 49 267.98 |
| $4s16d$ | 48 827.12 ± 0.10 | 48 827.16 | $4s56d$ | 49 269.42 ± 0.09 | 49 269.36 |
| $4s17d$ | 48 882.56 ± 0.07 | 48 882.50 | $4s57d$ | 49 270.71 ± 0.11 | 49 270.66 |
| $4s18d$ | 48 928.95 ± 0.09 | 48 928.92 | $4s58d$ | 49 271.92 ± 0.11 | 49 271.89 |
| $4s19d$ | 48 968.22 ± 0.07 | 48 968.22 | $4s59d$ | 49 273.12 ± 0.11 | 49 273.06 |
| $4s20d$ | 49 001.77 ± 0.07 | 49 001.79 | $4s60d$ | 49 274.29 ± 0.11 | 49 274.17 |
| $4s21d$ | 49 030.67 ± 0.09 | 49 030.69 | $4s61d$ | 49 275.58 ± 0.17 | 49 275.23 |
| $4s22d$ | 49 055.75 ± 0.07 | 49 055.73 | $4s62d$ | 49 275.87 ± 0.15 | 49 276.23 |
| $4s23d$ | 49 077.55 ± 0.07 | 49 077.56 | $4s63d$ | | 49 277.19 |
| $4s24d$ | 49 096.77 ± 0.04 | 49 096.70 | $4s64d$ | | 49 278.10 |
| $4s25d$ | 49 113.57 ± 0.04 | 49 113.57 | $4s65d$ | | 49 278.97 |
| $4s26d$ | 49 128.50 ± 0.04 | 49 128.51 | $4s66d$ | | 49 279.79 |
| $4s27d$ | 49 141.76 ± 0.04 | 49 141.80 | $4s67d$ | | 49 280.58 |
| $4s28d$ | 49 153.57 ± 0.04 | 49 153.66 | $4s68d$ | | 49 281.34 |
| $4s29d$ | 49 164.23 ± 0.04 | 49 164.30 | $4s69d$ | | 49 282.06 |
| $4s30d$ | 49 173.92 ± 0.06 | 49 173.87 | $4s70d$ | | 49 282.75 |
| $4s31d$ | 49 182.53 ± 0.04 | 49 182.52 | $4s71d$ | | 49 283.41 |
| $4s32d$ | 49 190.37 ± 0.05 | 49 190.34 | $4s72d$ | | 49 284.05 |
| $4s33d$ | 49 197.48 ± 0.05 | 49 197.46 | $4s73d$ | | 49 284.66 |
| $4s34d$ | 49 204.01 ± 0.05 | 49 203.93 | $4s74d$ | | 49 285.24 |
| $4s35d$ | 49 209.88 ± 0.05 | 49 209.85 | $4s75d$ | | 49 285.80 |
| $4s36d$ | 49 215.27 ± 0.05 | 49 215.28 | $4s76d$ | | 49 286.33 |
| $4s37d$ | 49 220.28 ± 0.05 | 49 220.25 | $4s77d$ | | 49 286.85 |
| $4s38d$ | 49 224.89 ± 0.05 | 49 224.83 | $4s78d$ | | 49 287.34 |
| $4s39d$ | 49 229.12 ± 0.05 | 49 229.06 | $4s79d$ | | 49 287.82 |
| $4s40d$ | 49 233.00 ± 0.05 | 49 232.96 | $4s80d$ | | 49 288.28 |

[a] MQDT calculated term values using parameters of Table IV(b).

[b] This state not included in least-squares fit.

[c] Term values from Ref. 4. Errors listed were used to weight the least-squares fit, and do not necessarily reflect the actual accuracy of this data.

[d] Reference 4 assigns a state at 46 308.257 $cm^{-1}$ to this configuration.

[e] Reference 4 assigns a state of 47 449.083 $cm^{-1}$ to the configuration $3d^2$. We have chosen the alternative assignment of $3d5s$ for this state, which is the $^1D_2$ state closest to $3d5s$ $^3D_2$, on the basis of mixing coefficients calculated in Sec. III D 2.

[f] See text: Sec. III D 2.

[g] Assigned in Ref. 4 as $3d5s$ $^1D_2$, at 48 083.383 $cm^{-1}$.

fied in the literature above the $4s12f$ state.[4] Thus, for high-lying Rydberg states, fields as low as ~10 V/cm are effective in the experimental elimination of parity as a good quantum number, allowing observable two-photon transitions from an "even" initial state to "odd" final states via Stark mixing of $^1S_0$ and $^1D_2$ states with the $^1P_1^o$ and $^1F_3^o$ states.

In order to reduce Stark effects, and also in order to obtain the best signal to noise, most of the data was taken with a 1 to 1.5 V potential between the parallel plates. Since at low fields the Stark effect is quadratic in the applied field, this eliminated the Stark effect as a measurable perturbation on the observed energy levels.

There are also pressure shifts of atomic energy levels due to the presence of foreign gases.[13] As

described in Ref. 1, shifts of $-0.8$ cm$^{-1}$/100 Torr were easily observed when Kr was used as a buffer gas. Neon, however, is known to have a much smaller pressure shift.[13] At 500 Torr a pressure shift of only 0.06 cm$^{-1}$ was observed in comparison with the signal from an oven containing 5 Torr of Ne. Neon, at pressures near 10 Torr, was thus used as the buffer gas during accurate wavelength measurements.

Systematic errors due to pressure shifts were minimized by maintaining equal pressures of buffer gas in each oven. In order to obtain adequate absorption depth for the higher members ($n^* > 30$) of the $^1P_1^0$ series, the Ca pressure in the reference oven had to be increased over that in the signal oven. This required that the temperature be raised from 700 to 800 C. No pressure shifts due to Ca could be observed even for temperatures of 900 °C.

We believe that systematic errors in the data presented in Tables I and II due to the above sources are less than 0.05 cm$^{-1}$.

### D. Mechanism of ionization

In order to elucidate the ionization mechanism, measurements were made of the dependence of the ionization signal on parameters such as laser intensity $I_L$, buffer gas pressure $P_b$, electric field $E$, and Ca vapor pressure $P_{Ca}$, which was a function of the temperature $T$. One of the most important observations was that for all of the observed two-photon resonances above 42 000 cm$^{-1}$, the ionization signal was proportional to $I_L^2$. This behavior persisted over three orders of magnitude in signal strength. At peak currents greater than about 1 $\mu$A, space-charge and/or electron-ion recombination effects resulted in saturation, i.e., in a less than quadratic dependence on $I_L$. The laser intensity required for saturation decreased as $P_{Ca}$ increased. Typically, for $P_{Ca} \sim 0.1$ Torr, saturation of the signal from $4s18s\,^1S_0$ occurred with $I_L = 10^5$ W/cm$^2$. Quadratic intensity dependence was also observed, as expected, when the energy of two laser photons exceeded the ionization energy of Ca.

The fact that both bound-state and continuum signals show the same intensity dependence implies that either (a) the ionization mechanism for bound states does not involve the absorption of a (third) photon, or (b) if photoionization is occurring in a measurable amount, it is totally saturated, i.e., it occurs with unit probability.

The relative signal strengths of bound-state resonances (above 48 000 cm$^{-1}$) and the continuum were found to be independent of the experimental parameters $I_L$, $P_{Ca}$, $P_b$, and $E$. The inability to enhance the intensity of the bound-state resonances relative to the continuum signal leads us to conclude that whatever the ionization mechanism is, it is already 100% efficient in this energy region.

For the lowest-energy state that we studied, the $4p^2\,^1D_2$ state at 40 720 cm$^{-1}$, the intensity dependence was found to increase towards a cubic dependence for $I_L < 5 \times 10^4$ W/cm$^2$, indicating that this state was being photoionized, i.e., that the overall process was three-photon photoionization. The ionization signal from the next-higher $^1D_2$ state, at 42 919 cm$^{-1}$, returned to the quadratic intensity dependence observed at all higher excitation energies.

Possible alternate mechanisms include Stark ionization[14] and collisional ionization (including the possibility of chemi-ionization[15]). Stark ionization appears unlikely in the fields (typically $<3$ V/cm) used, even for the highest Rydberg levels ($n^* \sim 60$) that we observed. Ionization by thermal collisions appears feasible for Rydberg states within an energy range $kT$ of the ionization threshold. (States with $n^* > 12$ were within $kT$ of the limit in our experiments.)

A "hot-wire" effect, in which the excited atom ionizes after collision with the probe or the wall of the oven, was eliminated by observing that the ion current pulse shape behaved identically for bound-state resonances and the continuum. This would not be expected for a process requiring excited atoms to diffuse to a surface before being ionized.

The long ion collection time (~1 msec) prevented us from studying the detailed time behavior of the ionization mechanism. Other experiments are planned with which we hope to elucidate the ionization mechanism.

### E. Measurement of relative intensities

If the ionization mechanism, and in particular its energy dependence, were understood, then the relative ionization signals observed could be converted into relative two-photon excitation cross sections.[16] And since the experiments[1] make use of essentially a single intermediate state, the two-photon cross sections could be related to the oscillator strengths of transitions from the intermediate state to the series of final two-photon states.

Although such determinations are not now possible, there are two features of the observed ionization signal strengths which probably can be related qualitatively to oscillator strengths at this time. In each case there is an unexpected dependence of signal strength on energy over a narrow energy range. These energy ranges are so small that it is unlikely that the ionization efficiency is varying appreciably.

The first feature occurs in a roughly 200 cm$^{-1}$ interval centered on 48 578 cm$^{-1}$. Within this inter-

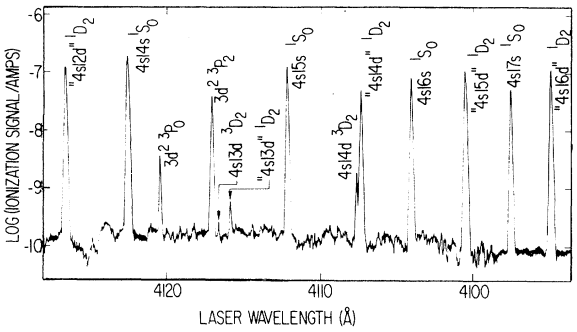


FIG. 4. Multiphoton ionization spectrum of states in the vicinity of the "$4s13d$" $^1D_2$ state at 48 578 cm$^{-1}$. Experimental conditions are those of Fig. 1. Note the appearance of the triplet states $3d^2\ ^3P_{0,2}$, $4s13d\ ^3D_2$, and $4s14d\ ^3D_2$.

val the $^1D_2$ ionization signal strength decreases by about 100 times, and then recovers its "normal value." This is shown in Fig. 4, which also shows no unusual behavior of the $^1S_0$ series at this energy. A possible explanation for this strong variation is that there is an interference between the transition moments of the various $^1D_2$ channels. This interference will be further complicated by the fact that this energy region is one in which the $^1D_2$ and $^3D_2$ series of $4snd$ cross. The bottom of the dip, at "$4s13d$," is also very close in energy to the $^3P_2$ state assigned to $3d^2$ by Risberg.[4] Thus triplet states from two configurations may be interfering with, and borrowing oscillator strength from, the $^1D_2$ series at this point.

The second feature is the remarkably slow decrease in $^1D_2$ signal strength over the 100 cm$^{-1}$ just below the ionization limit. This is shown in Fig. 1. By contrast, the strong decrease in the $^1S_0$ series strength in this energy range has roughly the $(n^*)^{-3}$ dependence expected. In Sec. III D 2 we will further discuss the $^1D_2$ strengths in terms of the wave functions which will be deduced there.

## III. MULTICHANNEL QUANTUM DEFECT THEORY

### A. Basic formulas

For convenience in the analysis which follows we summarize the working equations of MQDT, using the notation of Lee and Lu.[17]

The two most important attributes of a discrete Rydberg spectrum (characterized by the rigorous quantum numbers $J$ and parity) are the number, $M$, of interacting channels which contribute to the spectrum, and the number, $N$, of different series limits involved. The number of series limits is less than or equal to the number of interacting channels. We will explain later in this section how the numbers $M$ and $N$ are to be determined from experimental data.

First it will be useful to define two types of channels used in MQDT. We paraphrase from Ref. 3 Fano's general definition of a "collision channel." A collision channel describes a set of states that consists of an outer electron with arbitrary energy and a core in a definite energy level. Specification of the angular momenta of the outer electron and of the core, along with their coupling, completes description of the channel.

The set of states forming a collision channel does not diagonalize the electron-electron part of the Hamiltonian. There is, however, an alternate set of channels called "close-coupling" channels which does diagonalize the noncentral part of the electron-electron interaction. These close-coupled channels, the $\alpha$ channels, are derived by a unitary transformation from the collision channels. The two types of channels may or may not have different angular momenta coupling schemes; however, it is customary to ascribe $LS$ coupling to the $\alpha$ channels.

In this paper we will be concerned primarily with channels of even parity and $J=0$ or 2. For example, a collision channel with $J=0$ and even parity can be formed in the following ways, among others: an excited $s$ electron coupled to an $s$ core; an excited $p$ electron coupled to a $p$ core; or an excited $d$ electron coupled to a $d$ core. Of the many possible collision channels of the $^1S_0$ type, experiment shows that only two have any appreciable effect on the observed series of bound excited $^1S_0$ levels in Ca.

The number $N$ of series limits involved in the multichannel interaction picture is, simply stated, the number of distinct states of the core occurring in the channels which interact to produce the observed spectrum. For the $J=0$ even levels of Ca, the number of series limits is two, corresponding to collision channels $4sns$ and $4pnp$. For the $J=2$ even levels, the number of series limits is three, because channels occur for which the core is either the $4s$, or $4p$, or $3d$ configuration. The spin-orbit splittings of the $4p\ ^2P$ and $3d\ ^2D$ ion levels can be ignored when discussing bound states, since these splittings are very small compared to the energy differences between the $4s$, $3d$, and $4p$ states.

Each observed energy level has as many effective, principal quantum numbers $\nu_i$ assigned to it as there are series limits, $N$. The effective quantum numbers for a level of energy $E$ are determined from the relations

$$E = I_i - R/\nu_i^2 \ , \qquad (1)$$

where $I_i$ is the $i$th ionization limit, and where $R$ is the Rydberg constant. These $N$ equations determine $N-1$ independent relations of the form

$$I_i - R/\nu_i^2 = I_j - R/\nu_j^2, \quad i \neq j \ . \tag{2}$$

This set of $N-1$ equations determines a "line," called $\mathcal{L}$, in the $N$-dimensional space of the $\nu_i$; the line $\mathcal{L}$ plays an important role in determining the theoretical positions of the bound states, as will be explained shortly.

The $\nu_i$ are nonintegers, (except for hydrogen) and it is their nonintegral part which contains information about the mutual interactions between Rydberg series caused by electron-electron effects. It is therefore a characteristic feature of MQDT that the effective quantum numbers are, for many purposes, considered *modulo* 1. With this notation, the *quantum defect*, $\mu$, is given by the fractional part of $-\nu$, i.e., $\mu = -\nu \bmod 1$.

Beyond a radius $r_0$, the wave function of an excited state is represented as a superposition of the wave functions of collision channels, or so-called $i$ channels:

$$\Psi = \sum_{i=1}^{M} \phi_i \Big( f(\nu_i, l_i, r) \sum_{\alpha=1}^{M} U_{i\alpha} \cos(\pi\mu_\alpha) A_\alpha - g(\nu_i, l_i, r) \sum_{\alpha=1}^{M} U_{i\alpha} \sin(\pi\mu_\alpha) A_\alpha \Big) \ . \tag{3}$$

The functions $\phi_i$ are the wave functions of the core along with the angular part of the wave function of the excited electron in the $i$th collision channel. The functions $f$ and $g$ are the regular and irregular Coulomb wave functions for the $i$th channel. The quantities $\mu_\alpha$ are the eigenquantum defects of the close-coupled channels. Again, the $\alpha$ channels are derived from the collision, or dissociation, channels by the unitary transformation $U$. A principal aim of MQDT is to allow determination of this matrix from experiment. The $A_\alpha$ are determined from the boundary conditions which must be imposed on the wave functions in the three physically distinct regions: bound state, autoionizing state, or open continuum.

For the discrete spectrum, the behavior of the wave functions at $r \to \infty$ leads to the conditions

$$\sum_\alpha A_\alpha U_{i\alpha} \sin\pi(\nu_i + \mu_\alpha) = 0, \quad i = 1, \ldots, M \ . \tag{4a}$$

Note that although we use the same subscript, $i$, in $\nu_i$ and in $U_{i\alpha}$, there are only $N$ distinct values of $\nu_i$, whereas there are $M \geq N$ rows of $U$; see the text following Eq. (12). The set of homogeneous simultaneous equations (4a) for the $A_\alpha$ only has nontrivial solutions on the $N-1$ dimensional surface, $\mathcal{S}$, defined in $\nu_i$ space by

$$\det \left| U_{i\alpha} \sin\pi(\nu_i + \mu_\alpha) \right| = 0 \ . \tag{4b}$$

*The theoretical positions of the bound states are given by the intersection of the line $\mathcal{L}$ and the surface $\mathcal{S}$;* that is, the $\nu_i$ of the bound states are obtained as the simultaneous solutions of Eqs. (2) and (4b).

Expression (4b) defines a relation between the $\nu_i$ with the $\mu_\alpha$ and the $U_{i\alpha}$ as parameters. It is Eq. (4b) which must be fitted to experiment to determine the values of the eigendefects and the elements of the $U$ matrix.

### B. Analysis of the $^1S_0$ spectrum

The Ca spectra obtained using polarized laser excitation experimentally distinguished the $J=0$ states from those with $J=2$. Since it serves as an example of a simple two limit, two channel problem, the $J=0$ spectrum will be analyzed first. This analysis also serves to test the absolute accuracy of our measured term values by comparison with term values extrapolated from a least-squares fit of MQDT to previously measured $^1S_0$ term values.[4]

The $^1S_0$ bound-state spectrum of Ca consists of $4sns$ excitations converging on the first ($4s$) limit, $I_s = 49\,305.99$ cm$^{-1}$, with an interloper identified[4,5] as the $4p^2$ state. This interloper is the only bound member of the series $4pnp\ ^1S_0$ converging on the third $4p$ ionization limit, $I_p = 74\,609$ cm$^{-1}$. Even with the extensive new data reported in Ref. 1, there is no evidence in the bound-state spectrum for the presence of any other significant perturbation of the $^1S_0$ series.

Since the relevant channels for the $^1S_0$ spectrum, $4sns$ and $4pnp$, converge, respectively, on the $4s$ and $4p$ ionization limits, the appropriate Lu-Fano plot presents $\nu_s$ vs $\nu_p$. Figure 5 is such a plot

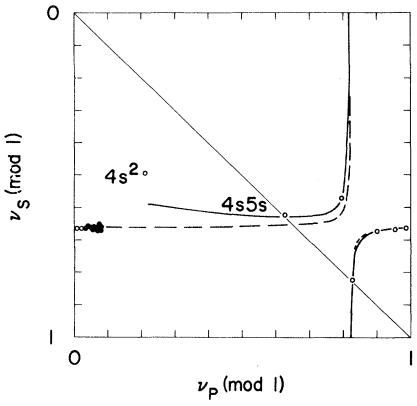


FIG. 5. Lu-Fano plot of $^1S_0$ data. The symbols are ○ for previously observed states (Ref. 4) and ● for the new data (Table I). The broken line is based on MQDT energy-independent parameters [Table III(a)] determined from a least-mean-squared fit to the data of Ref. 4. The solid curve is based on the MQDT energy-dependent parameters of Table III(b).

(see also Ref. 7), where open circles correspond to the previously observed $^1S_0$ states,[4] and the filled circles correspond to the new data (Table I). Note that in addition to plotting $\nu_s$ and $\nu_p$ modulo 1, we have followed the convention of inverting the axis for the lower limit effective quantum number so that the plot appears as $-\nu_s$ vs $\nu_p$ (modulo 1). In this plot an unperturbed $4sns$ Rydberg series would appear as a horizontal line, i.e., would have $\nu_s(\text{mod } 1) = \text{constant}$. This can be seen to be the case for most of the points plotted in Fig. 5, where the exceptions are the four lowest energy states. The presence of the $4p^2$ interloper causes the major perturbation, near $\nu_p(\text{mod } 1) = 0.8$, and penetration by the outer electron into the $4s$ ion core causes the deviation of the lowest energy ($4s^2$ and $4s5s$) states from the simple Rydberg formula.

The MQDT parameters needed to describe a two-channel problem are two eigendefects and a third parameter which defines the $2 \times 2$ unitary transformation matrix $U_{i\alpha}$. Following Ref. 18, this parametrization is accomplished by first sketching a curve through states of successively higher energy. Ignoring the $4s^2$ ground state, the curve is drawn such as to increase monotonically from lower left to upper right. The modulo 1 nature of the plot requires that a curve which has run off at one border must reappear at the opposite border. This sketched curve will be a first approximation to the curve, $\mathcal{S}$, defined by Eq. (4b). Once this curve is drawn, approximate values for the two eigendefects $\mu_s$ and $\mu_p$ are obtained by finding the intersections of $S$ with the $\nu_s = \nu_p$ diagonal, as in Ref. 19. These approximate values of the eigendefects are $\mu_1 = 0.37$ and $\mu_2 = 0.17$. Improvement of the $\mu_\alpha$ and initial determination of the $U_{i\alpha}$ are then carried out on a graphics computer terminal by trial and error. Further refinement of the parameters by least-squares fitting requires that theoretical term values be calculated for a given set of $\mu_\alpha$ and $U_{i\alpha}$.

The relation between $\nu_s$ and $\nu_p$ in Eq. (4b) can be written[19]

$$\nu_s = \nu_p - (1/\pi)\cot^{-1}\left[ U_{11}^2 \cot\pi(\nu_p + \mu_1) + U_{12}^2 \cot\pi(\nu_p + \mu_2) \right] . \quad (5)$$

For this case of two limits, the surface $\mathcal{S}$ of Eq. (4b) degenerates into the line of Eq. (5). The eigenstates of the system are then determined by simultaneously satisfying this relation and the condition [Eq. (2)], which for the present case is

$$E = I_s - R/\nu_s^2 = I_p - R/\nu_p^2 . \quad (6)$$

This is the line $\mathcal{L}$, and the eigenstates are found at the intersections of the lines $\mathcal{L}$ and $\mathcal{S}$ in the $\nu_s, \nu_p$ plot.

Approximate values of the intersections were found by using an analytically linearized $\mathcal{L}$ and a numerically linearized $\mathcal{S}$. These linearizations were carried out around the experimentally determined values of $\nu_p$. Since the calculated intersections only give $\nu_s(\text{mod}1)$, the integral part was supplied by the experimental term values.

The above algorithm was incorporated into a least-squares fitting program for refinement of the MQDT parametrization of the $^1S_0$ spectrum. The quantity minimized was the weighted sum of the squares of the $\text{cm}^{-1}$ deviations between calculated and measured term values. The weighting of the data was inversely proportional to the square of the estimated probable error associated with each data point. The nonlinear weighted least-squares fitting program used Marquardt's algorithm for combining the method of linearization of the fitting function with the method of a steepest-descent parameter search.[12] This program and all others described herein were written in APL and run interactively.

We applied this procedure to the $^1S_0$ data of Ref. 4 and 5, omitting the three lowest energy levels. The energies of these are affected by polarization of the ion core by the outer electron, and can only be described by MQDT with energy-dependent parameters. For the term values of Ref. 5, the rms deviation between measured and calculated values is 1.2 $\text{cm}^{-1}$. The largest deviation is due to the $4s12s$ state, where the measured value is 2.2 $\text{cm}^{-1}$ below the calculated value. By dropping this state from the fit, the rms error is reduced to 0.41 $\text{cm}^{-1}$. The more recently measured $^1S_0$ term values (to $4s11s$) of Ref. 4 are fit somewhat better, with a rms error of 0.17 $\text{cm}^{-1}$. The broken line curve in Fig. 5 is the graphical result of this fit.

Using the parameters from the least-squares fit of the Ref. 4 data, predicted term values were obtained for the $^1S_0$ series up to $4s32s$. Comparison of these predicted values and our measured values (Table I) yields an average error ($E_{\text{meas}} - E_{\text{calc}}$) of +0.09 $\text{cm}^{-1}$, and a rms error of 0.19 $\text{cm}^{-1}$. The average of the estimated experimental errors which appear in Table I is 0.14 $\text{cm}^{-1}$. This represents a clear verification of our wavelength determinations and of our estimates of both the systematic and relative errors in the data of Table I.

Next, the least-squares fit was extended to include the new high-lying states of Table I. The data were weighted in the least-squares fit by the estimated errors given in Table I, using the somewhat arbitrary error estimate of 0.1 $\text{cm}^{-1}$ for the data taken from Ref. 4. The weighted fit of the

combined data has a rms error of 0.10 $cm^{-1}$. The final MQDT parameters thus obtained are presented in Table III. The statistically estimated errors[12] in the last digit of each parameter are shown in parentheses in this and subsequent tables. The parameters given are, within the errors shown, identical to those obtained in the fit of Ref. 4 data alone.

In order to treat properly the lower-energy $^1S_0$ states, it is necessary to account for polarization of the ion core by the use of energy-dependent parameters. In treating the Ar spectrum, Lee and Lu[17] found that the $U_{i\alpha}$ matrix was essentially independent of energy; however, a linear energy dependence of the $\mu_\alpha$ eigendefects was required to fit the lower-energy states. Following their lead, a linear energy dependence was invoked for the $\mu_s$ eigendefect in an attempt to also fit the lower-energy states. Not surprisingly, a linear energy dependence was insufficient to fit the $4s^2$ ground state. Further, it could not fit the $4s5s$ state accurately without upsetting the fit of higher-energy members of the $^1S_0$ series. The result of a weighted least-squares fit, which omitted these two states, is shown as the solid curve in Fig. 5. Clearly the linear energy dependence invoked for $\mu_1$ reproduces the main trend of the low-energy data. The MQDT parameters and statistical error estimates are presented in Table III(b). Term values calculated using these parameters are given in the last column of Table I. The average error between these values and the measured term values is $-0.004$ $cm^{-1}$, with a rms distribution of 0.10 $cm^{-1}$.

In retrospect, the excellent fit of the $^1S_0$ spectrum by a two-channel MQDT model is unexpected. An additional channel that might be expected to play a role here, but for which there is no evidence within the bound-state spectrum, is the $3dnd\ ^1S_0$ channel. The lowest member of this series, which converges on the second, $I_d$, ionization limit, has the configuration $3d^2$. Since $3d^2\ ^3P_0$ and $^3P_2$ terms have been identified[4,5] as bound states, and since a $3d^2$ channel is seen in the $^1D_2$ spectrum,[1] the lack of evidence for a $3d^2\ ^1S_0$ state is quite surprising. Unless it interacts *extremely* weakly with the $4sns$ series, and has essentially zero oscillator strength from $4s4p$, this state does not lie in the energy range from $4s12s$ to the first ionization limit, which we have studied using multiphoton ionization spectroscopy. We think it equally unlikely that this state could lie lower in energy than $4s12s$ and not have been observed in previous studies of the Ca spectrum.[4,5] We must thus conclude that the $3d^2\ ^1S_0$ state is not bound, and that it exists, instead, as an autoionizing resonance somewhere above the first ionization limit.

TABLE III. MQDT parameters for $^1S_0$.

| (a) Energy independent | | |
|---|---|---|
| $\alpha$ | 1 | 2 |
| $\mu_\alpha$ | 0.3471(3) [a] | 0.171 756(7) |
| $U_{1\alpha}$ | 0.9810(3) | −0.194(2) |
| (b) Energy dependent | | |
| $\alpha$ | 1 | 2 |
| $\mu_\alpha$ | 0.3486(2) | 0.171 899(5) |
| $d\mu_\alpha/dE$ | 0.073(2) [b] | 0 |
| $U_{1\alpha}$ | 0.972 63(6) | −0.2324(3) |

[a] Estimated error in the last digit of each parameter is given in parentheses.

[b] The energy $E$ is normalized to the first ionization limit, $I_s$.

### C. Treatment of $N$ limits

Since it is known from previous work[1] that the $4snd\ ^1D_2$ series, which has the $4s$ state of the ion as its limit, is perturbed by $4p^2$, $3d5s$, and $3d^2$, that is, by series going to the $4p$ and $3d$ states of the ion, it is clear that we must deal with a three-limit version of MQDT in an attempt to analyze the $^1D_2$ bound states of Ca. The procedures used in Sec. III B must now be generalized, and we will make that generalization to the case of $N$ limits.

It is important to draw a distinction between different types of the $N$-limit problem based on whether one, or more than one, $\nu_i$ varies rapidly over the Rydberg series in question. This is equivalent to distinguishing between (a) cases where the lowest limit is well below all others and (b) cases where the lowest limit is not well removed from all other relevant limits.

The $^1D_2$ even-parity bound states of Ca are an example of case (a) where the three relevant limits are widely spaced (49 306, 62 987, and 74 609 $cm^{-1}$, respectively, for the $4s$, $3d$, and $4p$ states of the ion). The two limits associated with the $^2D$ state of the ion are to be treated as *one* limit in dealing with the *bound* states, since as long as $E < I_s$, the quantum numbers to the two $^2D$ limits are effectively identical. The same holds for the $^2P$ state of the ion; in each case we use the average of the two limits. An example of case (b) is furnished by the $J = 1$, odd-parity levels of Ca converging on the two $^2D$ limits at 62 956.24 and 63 016.93 $cm^{-1}$, as reported in Ref. 8.

The basic equations [Eq. (4)] apply, of course, in all cases, but the practical details of the fitting procedure are quite different in the two cases. In what follows, we will describe the case where the two lowest limits are well spaced; that is, the case for which only one $\nu_i$ is rapidly varying. Under these conditions the $N$-limit problem may be viewed as a set of $\frac{1}{2}N(N-1)$ two-limit problems. We have treated the case of closely spaced limits

as well, and will describe that procedure in a paper on the autoionizing spectra of Ca.

In applying the MQDT for $N$ limits, the first question is: Can approximate values of the eigendefects be obtained directly from experimental data, as is done in Ref. 19 for two limits? To answer this question, consider the basic equations (4a). They have $M$ sets of special solutions of the form

$$\nu_i = n_i - \mu_\beta, \quad A_\alpha = \delta_{\alpha\beta} ,$$

where the $n_i$ are integers and where $\beta$ is any one of the set $1, 2, \ldots, M$. The interpretation of these special solutions is that for all $\nu_i = \mu_\beta \pmod 1$, the wave function (3) reduces to a single $\alpha$-channel, hence the term "eigendefect." If we plot all possible solutions of this type modulo 1 in an $N$-dimensional cube, all points will lie on the body diagonal of the cube, i.e., on the line $\mathfrak{D}$.

$$\nu_1 = \nu_2 = \nu_3 = \cdots = \nu_N . \tag{7}$$

*The intersections of this line* $\mathfrak{D}$ *with the periodic surface,* $\mathfrak{S}$, *give the eigenquantum defects,* $\mu_\alpha$. There are just $M$ distinct eigendefects. However, since one does not know the surface $\mathfrak{S}$ *a priori*, one cannot determine the $\mu_\alpha$ from the intersections of $\mathfrak{D}$ and $\mathfrak{S}$.

This is the essential difficulty of the $N$-limit problem for $N > 2$. That is, the data only allow one to construct a one dimensional curve in $N$ space. And although this curve lies in the surface $\mathfrak{S}$, it alone does not permit construction of $\mathfrak{S}$. Figure 6 is a stereo view of this line for the $^1D_2$ states of Ca. The question is whether any projection of this line on to the various $(\nu_i, \nu_j)$ planes can be used to find starting values of the $\mu_\alpha$.

We start by making plots of the data on the various relevant unit squares, such as Figs. 7(a)–7(c). The number of such plots is $\frac{1}{2}N(N-1)$, and each is equivalent to viewing the entire data as if they were part of a two-limit problem. For $N$ dimensions the projection of the "body" diagonal $\mathfrak{D}$ on any one of these planes is the "face" diagonal of the unit square on that plane. In the prescription of Lu and Fano,[18] *for two limits* it is the intersections of these face diagonals with lines connecting the data points (in order of increasing energy) which give rough values for the eigendefects, and, of course, the number of channels $M$, as well. On any one of the $\frac{1}{2}N(N-1)$ planes there will be up to $M$ intersections between the face diagonal and the hand-drawn curves passing through the data points (of each series) in order of decreasing energy from the limit. Hence, there will be up to $\frac{1}{2}MN(N-1)$ possible values of eigendefects determined by these crossings. The plane on which the largest number of intersections is seen gives a lower limit to the number of channels which is re-

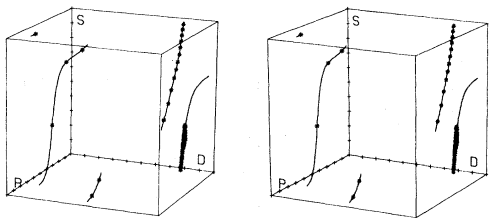


FIG. 6. Stereo view of line connecting observed $^1D_2$ states. The axes labeled $S$, $D$, and $P$ correspond to $-\nu_s$, $\nu_d$, and $\nu_p$, respectively, all plotted mod 1. If a stereo viewer is not available, view the figure as follows: Hold the figure about a foot from your eyes and place a piece of cardboard between your eyes so that each eye can see only one image; then fuse the two images.

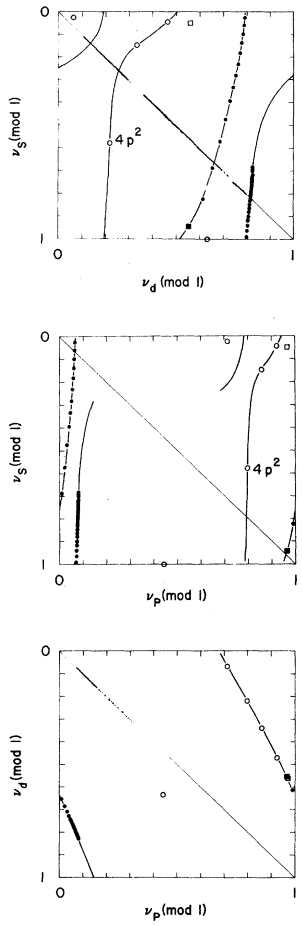


FIG. 7. Lu-Fano plots of $^1D_2$ states. The symbols are ○ for previously observed states (Ref. 4) and ● for the new data (Table I), with the exceptions that □ is the state labeled by $4s7d$ in Ref. 4 and ■ is the state that we identify as $4s7d$. The solid curves are MQDT fits based on the parameters of Table IV(a).

quired to describe the series under study.

For the commonly occurring case where each perturbing series interacts with the main series in a different energy range, the correct choice of starting values for the eigendefects is as follows. For convenience, we label a branch of the hand-drawn curves by the perturbing level it contains, even though states on the branch are in fact a mixture of $i$ and $\alpha$ channels. For example, the $4p^2$ branch is indicated in Figs. 7(a) and 7(b). The eigendefect of this branch is to be found from the intersection of the diagonal line and that branch on the plot of $-\nu_s$ vs $\nu_p$ in Fig. 7(b), i.e., from the plot involving *the limit of the series to which the perturber belongs*, and is about 0.21. The eigendefect of the $3dns$ branch, therefore, is to be read from the plot of $-\nu_s$ vs $\nu_d$ in Fig. 7(a), and is seen to be approximately 0.35. Similarly, we suppose that the third vertical branch in Fig. 7(a) is due to the configuration $3d^2$. If our assignment of the channel core is correct, the eigendefect for that branch is also to be found from Fig. 7(a) and is approximately 0.18.

This method for sorting out the true set of eigendefects will not work if the assignments and energies of at least some of the perturbers are not known in advance. This underscores the dependence of the MQDT method on previous spectroscopic work.

There remains a fourth eigendefect to be determined for the $^1D_2$ states. It corresponds very roughly to the defect of the unperturbed $4snd$ series. It has a value of about 0.9 if read from the top-left-most branch in Fig. 7(a), and a value of 0.8 if read from the corresponding branch in Fig. 7(b). Since there are few data points corresponding to bound states on this curve, and since the states which do lie on it are so far from the ionization limit that the defect may be energy dependent, we cannot expect to obtain a very good value for this eigendefect.

Once approximate values of the $\mu_\alpha$ are found, one must determine the elements of the $M\times M$ unitary matrix $U_{i\alpha}$ that transforms the close-coupled channels into the collision channels. This matrix will have $\frac{1}{2}M(M-1)$ independent elements. These are to be chosen so that the theoretical surface, $\mathcal{S}$, in fact contains the line (Fig. 6) through the experimental data. This will be done by choosing $\mathcal{S}$ so that, when properly projected on planes, it reproduces the curves of Fig. 7.

We now discuss how to obtain such theoretical curves. Recall that Eq. (4b) defined the $(N-1)$-dimensional surface $\mathcal{S}$. Moreover, from the $N$ relations (1) we saw that one can obtain $(N-1)$ *independent* relations (2), which determined the line $\mathcal{L}$. According to MQDT, the theoretical positions of the bound states of the system are found from the effective quantum numbers $\nu_i$, which simultaneously satisfy Eqs. (2) and (4b). That is, the bound states occur at the intersections of the line $\mathcal{L}$ and the surface $\mathcal{S}$.

For the case $N=3$, as in Ca, the Eqs. (2) are

$$\nu_s = G(\nu_d) = \{-[(I_d - I_s)/R] + \nu_d^{-2}\}^{-1/2} , \tag{8a}$$

$$\nu_p = H(\nu_d) = \{[(I_p - I_d)/R] + \nu_d^{-2}\}^{-1/2} . \tag{8b}$$

We solve Eq. (4b) to obtain

$$\nu_s = F(\nu_d, \nu_p) . \tag{9}$$

Now consider the function

$$\nu_s = F(\nu_d, H(\nu_d)) \equiv \bar{F}(\nu_d) . \tag{10}$$

This determines a curve in the $(\nu_s, \nu_d)$ plane. But Eq. (8a) is also a curve in the $(\nu_s, \nu_d)$ plane. *The intersections of these curves give the coordinates of the simultaneous solutions to Eq. (8) and (9) giving the positions of the bound states.* Thus Eq. (10) will be a suitable theoretical curve with which to compare data in the $(\nu_s, \nu_d)$ plane. It is important to note that although $\mathcal{S}$ is strictly periodic in $N$ dimensions, the projections such as Eq. (10) are *not* periodic. The analogous theoretical curve in the $(\nu_s, \nu_p)$ plane is

$$\nu_s = F(H^{-1}(\nu_p), \nu_p) , \tag{11}$$

where $H^{-1}$ is the inverse of the function defined in Eq. (8b). All the above considerations and procedures are obviously generalizable to more than three limits.

### D. Analysis of the $J=2$, even bound states of Ca

We now apply the techniques of Sec. III C to analysis of the two bound Rydberg series of Ca which have $J=2$ and even parity. These two series are nominally "$4snd$." We have already seen that there are three limits involved, so $N=3$. The next job is to enumerate the $M$ channels and decide on the labeling of collision and close-coupled channels.

The choice of labels should reflect the interactions between channels. These interactions are embodied in the $U$ matrix and have two principal causes. First, there is mixing due to the interaction of different configurations; second, there is mixing, within a given configuration, due to the recoupling of spin and orbital angular momenta. In general both effects will be present.

However, in the cases of Ar and Xe,[17,19] it was found that recoupling played a predominant role, with configuration mixing being a small perturbation on the recoupling. Lee and Lu[17] expressed this physical situation by writing $U_{i\alpha} = \sum_{\bar{\alpha}} U_{i\bar{\alpha}} V_{\bar{\alpha}\alpha}$, where $U_{i\bar{\alpha}}$ is the analytically known transformation from $LS$ to $jj$ coupling, with the $\bar{\alpha}$ channels

$LS$ coupled and belonging to pure configurations. The $V_{\bar{\alpha}\alpha}$ matrix, representing the weak configuration mixing, was nearly diagonal and transformed between pure-configuration $LS$-coupled channels ($\bar{\alpha}$) and mixed-configuration channels ($\alpha$) for which $L$ and $S$ were useful labels but not exact quantum numbers.

We have found that Ca is at the other extreme from Ar and Xe in that the channel mixing is due essentially to configuration interactions, with no observable recoupling effects on the energy levels. That is, the already known and classified bound states separate cleanly into singlets and triplets, as do the many newly observed states reported in Ref. 1. The curves through the experimental quantum defects show no avoided crossings between singlets and triplets. Therefore, as far as the determination of energy levels is concerned, we may take the collision channels (which have well defined configurations of core and excited electrons) to be $LS$ coupled. The $U$ matrix then describes the transformation between these $LS$-coupled collision channels and a set of mixed-configuration $\alpha$ channels for which $L$ and $S$ are still suitable labels. The $LS$-$jj$ recoupling matrices for the configurations $sd$, $ds$, $dd$, and $pp$ are not required for discussing the bound $J=2$ even spectrum of Ca. The absence of recoupling effects in Ca is because (a) the first ionization limit is an $S$ state, without spin-orbit splitting, and (b) the spin-orbit splitting of the first excited states of the ion $^2D_{3/2,5/2}$ has the very small value of 60 cm$^{-1}$ relative to the 14 000 cm$^{-1}$ separation of the $^2S$ and $^2D$ limits. (Recoupling will play a role in the autoionizing spectra of Ca.) Recoupling effects will also be present and increasingly important in the spectra of Sr, Ba, and Ra.

The $LS$-coupled collision channels with $J=2$ from the configurations $4snd$, $3dns$, $3d^2$, and $4p^2$ comprise ($^1D_2$, $^3D_2$), ($^1D_2$, $^3D_2$), ($^1D_2$, $^3P_2$, $^3F_2$), and ($^1D_2$, $^3P_2$). However, the channels $^3P_2$ and $^3F_2$ from $3d^2$, and the channel $^3P_2$ from $4p^2$ are not needed because there is no evidence that they perturb either Rydberg series. We consider both singlet and triplet channels because in our experiments there are energy regions where both series are seen in the ionization signal, even though they do not perturb each other.

Because singlets and triplets do not interact, the $U$ matrix will have many zero entries, and its rows and columns may be labeled in such a way that it is block diagonal. This results in a great mathematical simplification. The determinant to be worked out [Eq. (4b)] factors into two determinants, one $4\times4$, the other $2\times2$, and we can separately analyze the singlet and triplet spectra. It may be that at a later stage of the analysis one will have to account for the coupling between the singlet and triplet channels in order to account for fine details of the spectrum, particularly the oscillator strengths of the $^3D_2$ lines.

We are now in a position to list all the channels which are relevant to an analysis of the two observed Rydberg series from "$4snd$." The six collision channels and their associated configurations (with core electron listed first) are as follows:

| $i=$ | 1 | 2 | 3 | 4 | 5 | 6 |
|---|---|---|---|---|---|---|
| | $4snd$ | $3dns$ | $3dnd$ | $4pnp$ | $4snd$ | $3dns$ |
| | $^1D_2$ | $^1D_2$ | $^1D_2$ | $^1D_2$ | $^3D_2$ | $^3D_2$ |

The $\alpha$ channels do not have definite configurations associated with them. However, for Ca these channels are approximately $4snd$, $3dns$, $3dnd$, $4pnp$, $4snd$, and $3dns$ for $\alpha=1$–$6$, respectively. Channels $\alpha=1$, 2, 3, 4 are $^1D_2$, while channels $\alpha=5$, 6 are $^3D_2$.

### 1. Singlets

We now apply the techniques outlined in Sec. III C to analyze in detail the $4snd$ $^1D_2$ series of Ca.

We consider Eq. (4a) with $M=4$;

$$\sum_{\alpha=1}^{4} A_\alpha U_{i\alpha} \sin\pi(\nu_i+\mu_\alpha)=0 \ , \tag{12}$$

where the $\nu_i$ are labeled

$$\nu_1=\nu_5=\nu_s, \quad \nu_2=\nu_3=\nu_6=\nu_d, \quad \nu_4=\nu_p \ .$$

Following Lu[19] we introduce the new variables $B_1$, $B_4$ such that

$$A_\alpha=[\sin\pi(\nu_d+\mu_\alpha)]^{-1}\sum_{j=1,4} U^\dagger_{\alpha j}B_j \ . \tag{13}$$

Because of the orthogonality of different rows of $U$, Eqs. (12) with $i=2,3$ are satisfied identically, and the above substitution reduces Eq. (12) to

$$\sum_{j=1,4} B_j \sum_{\alpha=1}^{4} U_{1\alpha}\frac{\sin\pi(\nu_s+\mu_\alpha)}{\sin\pi(\nu_d+\mu_\alpha)}U^\dagger_{\alpha j}=0 \ ,$$

$$\sum_{j=1,4} B_j \sum_{\alpha=1}^{4} U_{4\alpha}\frac{\sin\pi(\nu_p+\mu_\alpha)}{\sin\pi(\nu_d+\mu_\alpha)}U^\dagger_{\alpha j}=0 \ . \tag{14}$$

Since

$$\frac{\sin\pi(\nu_i+\mu_\alpha)}{\sin\pi(\nu_k+\mu_\alpha)}=\sin\pi(\nu_i-\nu_k) \times[\cot\pi(\nu_k+\mu_\alpha)+\cot\pi(\nu_i-\nu_k)] \ , \tag{15}$$

we can expand the determinant of (14) and solve for $\nu_s$ to obtain

$$\nu_s = F(\nu_d, \nu_p)$$

$$= \nu_d + \frac{1}{\pi}\cot^{-1}\left(\frac{[\sum_\alpha U_{1\alpha}U_{4\alpha}\cot\pi(\nu_d+\mu_\alpha)]^2}{\cot\pi(\nu_p-\nu_d)+\sum_\alpha U_{4\alpha}^2\cot\pi(\nu_d+\mu_\alpha)} - \sum_\alpha U_{1\alpha}^2\cot\pi(\nu_d+\mu_\alpha)\right), \quad (16)$$

which defines the function $F$ of Eq. (9).

The theoretical positions of the bound $^1D_2$ states occur at the simultaneous solution of Eqs. (8) and (16), except that there is a lowest crossing below whose energy further crossings do not correspond to real states.

As described previously, to project the solution of this combined system on the $(\nu_s, \nu_d)$ plane, or on the $(\nu_s, \nu_p)$ plane, one plots $\nu_s = F(\nu_d, H(\nu_d))$ or $\nu_s = F(H^{-1}(\nu_p), \nu_p)$, respectively.

The solid curves in Fig. 7 are $F(\nu_d, H(\nu_d))$ for the values of eigendefect and $U$ given in Table IV(a).

The numerical values in Table IV were obtained by a combination of inspection and least-squares fitting, similar to the $^1S_0$ analysis. We found that the bound-state data could be fit accurately by setting $U_{32} = U_{42} = U_{43} = 0$ and adjusting the remaining three parameters in $U$. Setting these elements of $U$ equal to zero might be thought to imply a lack of mutual interaction between the perturbing channels. Rather it reflects the fact that since there is only one bound member of each perturbing series ($3d5s$, $3d^2$, and $4p^2$), the data are insufficient to determine their mutual interactions. One may say that the choice of zeros in $U$ defines the MQDT model we are using. The interactions between perturbers will, of course, be obtainable from the autoionization spectra.

Given the choice of zero elements, the magnitudes of the remaining elements of $U_{i\alpha}$ are uniquely determined by the fit to experiment. The signs of the off-diagonal elements were determined following the convention of Appendix B of Ref. 17, in which an $M \times M$ unitary matrix is generated from $\frac{1}{2}M(M-1)$ elementary rotations. Since $M=4$, there are six independent rotation angles, but three are zero by our choice of the zeros in $U$. The matrix of Table IV(a) is generated by successive rotations through angles of 0.4800, 0.343, and 0.135 radians, respectively. If the relative signs of these angles are changed, there are changes in sign of various elements of $U$, but no changes in magnitudes. We have verified that all combinations of the signs of these three angles lead to identical channel curves, Fig. 7, as well as to identical values of the squared mixing coefficients to be discussed in Sec. III D 2.

The fit is seen to be very good, except for the single point marked with an open square and the two lowest lying levels, which can be fitted by invoking a small energy dependence in the $\mu_\alpha$. However, the fit of the open square point cannot be improved by any reasonable energy dependence of the parameters. This point is given by the highest $^1D_2$ term value (labeled $4s7d$) resolved by Risberg in Ref. 4. Our original work[1] did not cover the energy range below 46 830 cm$^{-1}$, and so we did not at first have an energy for the $4s7d$ state obtained by multiphoton ionization spectroscopy. However, we repeated our experiment in the lower-energy range and obtained the result shown in Fig. 8.

The position marked with the arrow in Fig. 8 is where Risberg's $4s7d$ $^1D_2$ state should have appeared. Instead we found a $^1D_2$ state at 46 199.2 cm$^{-1}$ and it is our identification of the $4s7d$ state. This state appears in Fig. 7(a) as a filled square

TABLE IV. MQDT parameters for $^1D_2$.

(a) Energy-independent parameters

| $\alpha$ | | 1 | 2 | 3 | 4 |
|---|---|---|---|---|---|
| $\mu_\alpha$ | | 0.818 (2)[a] | 0.3367(2) | 0.1843(1) | 0.2050(3) |
| $U_{i\alpha}$ | $i=1$ | 0.8277(8) | −0.4618(6) | −0.298 (2) | −0.113 (4) |
| | 2 | 0.4309(7) | 0.8870(3) | −0.1554(9) | −0.059 (2) |
| | 3 | 0.333 (2) | 0 | 0.9417(6) | −0.045 (2) |
| | 4 | 0.135 (4) | 0 | 0 | 0.9909(6) |

(b) Energy-dependent parameters

| $\alpha$ | | 1 | 2 | 3 | 4 |
|---|---|---|---|---|---|
| $\mu_\alpha$ | | 0.801 (1) | 0.3375(2) | 0.1840(1) | 0.2130(1) |
| $d\mu_\alpha/dE$ | | 0.439 (7)[a] | 0 | 0 | 0 |
| $U_{i\alpha}$ | $i=1$ | 0.8096(5) | −0.4590(4) | −0.307 (1) | −0.2000(7) |
| | 2 | 0.4183(5) | 0.8884(2) | −0.1583(7) | −0.1033(4) |
| | 3 | 0.335 (1) | 0 | 0.9386(5) | −0.0827(4) |
| | 4 | 0.2398(8) | 0 | 0 | 0.9708(2) |

[a] See notes to Table III.

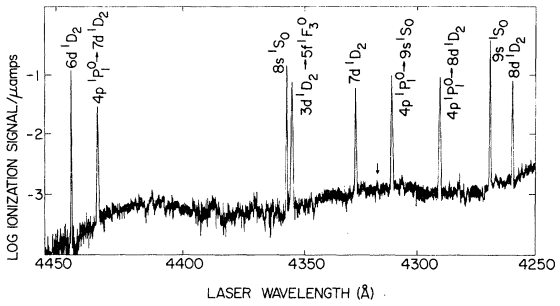


FIG. 8. Multiphoton ionization spectrum showing the $4s7d\ ^1D_2$ state at 46 199 cm$^{-1}$. The arrow marks the position where this state should have appeared according to Ref. 4. Some of the peaks correspond to transitions from intermediate states populated by absorption in the wings of the collision-broadened lines.

and is seen to be in very good agreement with theory, as are all the other states except the two lowest in energy.

### 2. *Wave functions*

Having obtained good values of the eigendefects and transformation matrix, we are in a position to calculate the expansion coefficients[17] $Z_i$ by means of which the wave function $\Psi$ of a given bound state is expressed in terms of the collision channel wave functions.

In Figs. 9(a)–9(c) we give the fractional admixture of channels $i=2,3,4$ in the bound states of the nominally $4snd\ ^1D_2$ series. The calculation of these coefficients follows closely Ref. 17, especially Eq. (2.11) of that reference, which contains a misprint, and should read instead

$$Z_i^{(n)} = (-1)^{l_i+1}\nu_i^{3/2}\sum_\alpha \frac{U_{i\alpha}\cos\pi(\nu_{i,n}+\mu_\alpha)A_\alpha^{(n)}}{N_n}\ , \tag{17}$$

where $N_n$ is a normalization factor defined in Eq. (2.8) of Ref. 17, and where $n$ labels the bound states.

In Figs. 9(a)–9(c) the admixtures are plotted versus $\nu_s$. The parameters of Table IV(a) have been used in obtaining the mixing coefficients for all but the two lowest lying states of the series.

Figure 9(a) shows the admixture of the $4pnp$ configuration into the $^1D_2$ series; it is very strongly localized in the vicinity of the state $A$ already labeled $4p^2$ in earlier work. However, as shown in Fig. 9(b), the admixtures of the $3dns$ and $3dnd$ configurations are by no means confined to a small number of states. Curiously, the state at 47 449 cm$^{-1}$ [$B$ in Fig. 9(b)] labeled in Ref. 4 as $3d^2\ ^1D_2$, is found in this analysis to have zero $3dnd$ character, and the state at 48 083 cm$^{-1}$ [$C$ in Fig. 9(b)] labeled $3d5s$ in Ref. 4, is well off the peak of the $3dns$ admixture curve. If we were to assign the label $3d5s$ to any state, it would be either to the state at 47 449 cm$^{-1}$ ($B$), as is done in Table II, or to the next lower state at 46 949 cm$^{-1}$. From Fig. 9(b) it is clear that although there are some 40 members of the $^1D_2$ series which have significant admixtures of the $3dnd$ channel, there is no state which has more than about 4% $3dnd$. Thus, although the $3d^2$ configuration is seen to have appreciable effects on the series as a whole, there is no state which "deserves" the label $3d^2\ ^1D_2$. For

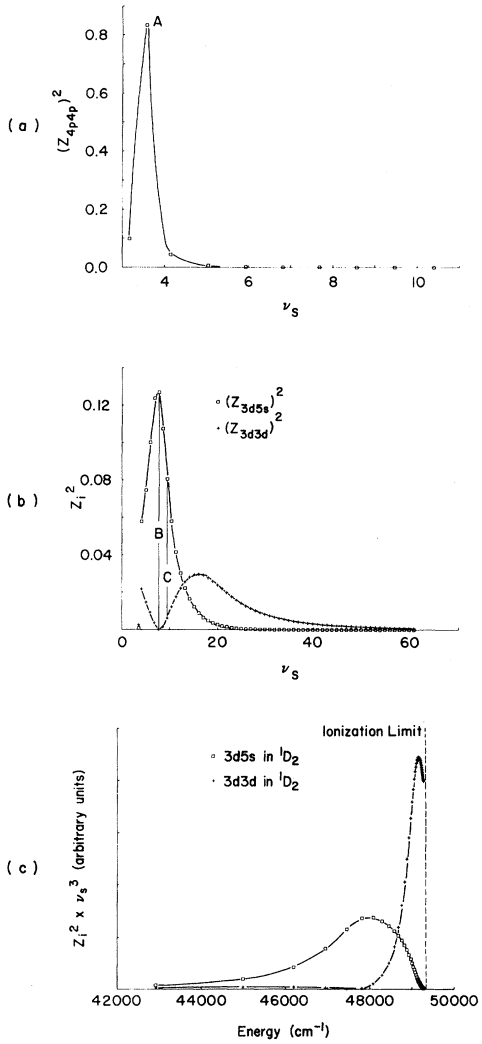


FIG. 9. Fractional admixture of collision channels (other than $4snd$) in the bound $^1D_2$ states. (a) Admixture per state: the state labeled $A$ contains most of the $4p^2$ configuration; (b) admixture per state: the state labeled $B$ is the state with the highest amount of $3d5s$ character, whereas the state labeled $C$ was called $3d5s$ in Ref. 4; (c) admixture per unit energy (arbitrary units) of the $3d3d$ and $3d5s$ states into the bound-state region.

the convenience of the user of Table II, the $^1D_2$ states above 47 449 cm$^{-1}$ are labeled $4snd$ with $n$ integral. Note that no state is labeled $3d^2$. Our labeling of the $3dns$ and $3dnd$ channels will be discussed after we treat the $^3D_2$ spectrum in Sec. III D 3.

The sum of the $(Z_{3d5s})^2$ over the bound states is 1.02, thus accounting fully for this interloper; however, the sum over bound states of $(Z_{3d3d})^2$ is only 0.63. If we express the mixing coefficients per unit energy [as shown in Fig. 9(c)], we find the "center of gravity" of the $3d5s$ and $3d^2$ states at about 48 000 and 49 150 cm$^{-1}$, respectively. This shows that a substantial part of $3d^2\ ^1D_2$ lies in the autoionizing spectrum just above $I_s$.

Furthermore, this admixture of $3dnd$ in $4snd$ near $I_s$ accounts qualitatively for the fact that the signal strength of the bound $^1D_2$ levels falls off much less rapidly than $(n^*)^{-3}$, as expected from quantum defect theory and as seen approximately for $4sns\ ^1S_0$ (see Fig. 1).

This completes the discussion of the $^1D_2$ series insofar as the determination of mixing coefficients, eigendefects, and the $U$ matrix are concerned. We next turn to the $^3D_2$ states.

### 3. Triplets

Only a few members of the $^3D_2$ spectrum were seen by multiphoton ionization spectroscopy, since the ground state of the two-photon transition is a singlet, and $LS$ coupling well describes Ca. However, in certain energy regions the $^1D_2$ and $^3D_2$ series come quite close together, and the Lu-Fano plots show regions where the singlet and triplet channels seem to cross. This is shown in Fig. 10.

Although the singlet and triplet channels do not in fact cross, the bound states are not dense enough to show the detail of the avoided crossings. We have just seen that it is not necessary to take the triplets into account to fit the bound-state $^1D_2$ data to theoretical curves.

The solid curves through the triplet states in Fig. 10 were calculated from a formula similar to Eq. (5) using the eigendefects and $U$ matrix shown in Table V.

A two-channel description of the $^3D_2$ $4snd$ series is a very good one, at least in the absence of data above $4s17d$.

We can now discuss our labeling of the $3dns$ and $3dnd$ $^1D_2$ branches. There is no *a priori* reason to assign $3dns$ and $3dnd$ to the branches with eigendefects 0.337 and 0.184, respectively, rather than *vice versa*. However, in the triplet spectrum there is no branch from $3d^2$, so the assignment of 0.339 to the $3dns$ branch of $^3D_2$ is unambiguous. We note that this is very near to the eigendefect of the

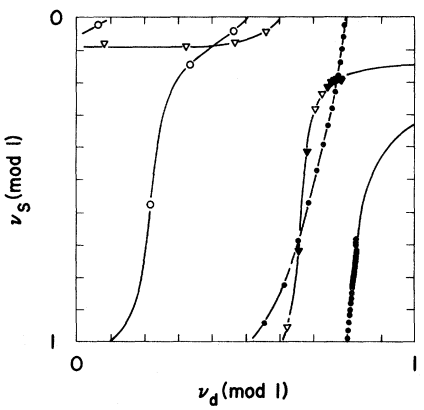


FIG. 10. Lu-Fano plot of all $J=2$ states. The symbols are ○ for previously observed $^1D_2$ states, ● for new $^1D_2$ states, ▽ for previously observed $^3D_2$ states, (see Refs. 4 and 6), and ▼ for $^3D_2$ states observed in our spectra. The solid curves are calculated from MQDT using the parameters of Table V for the triplets and Table IV(a) for the singlets.

branch we labeled $3dns$ in $^1D_2$. Furthermore, we have made a two-channel fit to the bound $^3D_1$ even states[4] of Ca and find $\mu_{3dns}=0.341$. Since Lu pointed out in Sec. VIII of Ref. 19 that the character of approximately $LS$-coupled $\alpha$ channels is nearly independent of $J$, we have used the near identity of the three eigendefects to assign $3dns$ in $^1D_2$ to the branch with $\mu=0.337$.

For completeness, we note that the full set of parameters for $^3D_1$ determined from the data of Ref. 6 is $\mu_1=0.8691(3)$, $d\mu_1/dE=0.183(3)$, $\mu_2=0.34102(4)$, and $U_{12}=-0.2765(3)$.

## IV. DISCUSSION

We now discuss several questions which arise when one tries to extend this MQDT treatment to a wider energy range. First, how is the Pauli exclusion principle to be applied to "$3d^2$" $^3D_2$ when, in MQDT, the two $d$ electrons have different noninteger principal quantum numbers and hence different radial wave functions?

We must have the answer to this question in order to include $3dnd\ ^3D_2$ in the autoionizing region without having it present as a false (unphysical)

TABLE V. MQDT (energy-dependent) parameters for $^3D_2$.

| $\alpha$ | 1 | 2 |
|---|---|---|
| $\mu_\alpha$ | 0.8696(6) [a] | 0.3390(1) |
| $d\mu_\alpha/dE$ | 0.176(5) | 0 |
| $U_{1\alpha}$ | 0.9640(1) | −0.2660(5) |

[a] See note to Table III.

channel in the bound-state region, where it would correspond to $3d^2\,{}^3D_2$.

More generally, since the surface $s$ is strictly periodic, channels required for analysis of a higher-energy region always appear at low energy as well, even though there are no observed states of these channels at low energy.

For example, if the curve plotted in Fig. 7 [determined by Eq. (8b) and (16)] is extended below $4s4d$ into the region where $\nu_d$ lies between one and two, there will be three additional states predicted by the crossings with Eq. (8a). These would be members of the $3dnd$, $3dns$, and $4snd$ series, in order of decreasing energy. But in fact, there is only one real ${}^1D_2$ state in this region, namely, $4s3d$.

This difficulty is shown in Fig. 11. The function given by Eqs. (8b) and (16) was evaluated using the energy-dependent parameters of Table IV(b). The dotted lines are Eq. (8a), and the crossings give the positions of the states. The $4s3d$ state is closest in energy to Crossing $A$. Crossing $B$ corresponds to the $4s4d$ state. But the crossings $C$ and $D$ do not correspond to any real states, and exemplify the difficulty being discussed.

By invoking a quadratic energy dependence of $\mu_2$ and $\mu_3$ we are able to move these channels out of the way, avoid unphysical crossings, and fit the two lowest states. However, the precise quadratic energy dependence is not well determined, and the fit to the high-lying states is somewhat impaired.

Thus the energy dependence of eigendefects for channels describing series going to higher limits are not uniquely determined from bound-state data. Only when the relevant autoionizing spectra are known and analyzed can these energy dependences be uniquely specified.

We have seen that the three-limit version of MQDT gives a thorough description of the $J=0$ and 2 even-parity bound spectra of Ca, unifying the excellent data of Risberg[4] obtained by emission spectroscopy with the new data obtained by multiphoton ionization spectroscopy. Use of multiphoton ionization spectroscopy to study autoionization spectra will make full use of the $N$-limit formulas given here and will help resolve the questions about MQDT discussed above. Work on the $J=0$ and 2 spectra of Sr and on the even-parity autoionizing spectra of Ca is well under way and will be reported shortly.

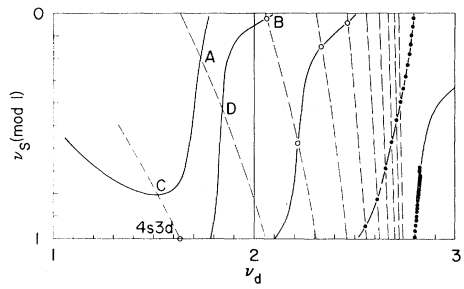


FIG. 11. Lu-Fano plot on an extended $\nu_d$ scale. The solid curve results from Eqs. (8b) and (16) plotted with the parameters of Table IV(b). The dotted lines are Eq. (8a). The $4s3d$ state is closest in energy to crossing $A$. Crossing $B$ corresponds to the $4s4d$ state. Crossings $C$ and $D$ do not correspond to real states.

ACKNOWLEDGMENTS

We are grateful to Professor U. Fano for introducing us to MQDT and to Dr. K.-T. Lu for several helpful discussions. We thank Dr. P. Camus for giving us his unpublished data on the ${}^3D_2$ states of Ca. Mr. L. H. Manganaro gave able technical assistance in all phases of the experimental work.

*Supported in part by the U.S. Army Research Office.
[1]P. Esherick, J. A. Armstrong, R. W. Dreyfus, and J. J. Wynne, Phys. Rev. Lett. 36, 1296 (1976).
[2]M. J. Seaton, Comments At. Mol. Phys. D 2, 37 (1970); also Proc. Phys. Soc. (Lond.) 88, 801 (1966).
[3]U. Fano, J. Opt. Soc. Am. 65, 979 (1975); K. T. Lu, Phys. Rev. A 4, 579 (1971).
[4]G. Risberg, Ark. Fys. 37, 231 (1968).
[5]C. E. Moore, *Atomic Energy Levels, Vol. I*, NBS(US) Circular No. 467 (U.S. GPO, Washington, D.C., 1949).
[6]P. Camus, private communication and unpublished.
[7]K. T. Lu, J. Opt. Soc. Am. 64, 706 (1974).
[8]C. M. Brown, S. G. Tilford, and M. L. Ginter, J. Opt. Soc. Am. 63, 1454 (1973).
[9]I. Itzkan and F. Cunningham, IEEE J. Quant. Elect. QE-8, 101 (1972).
[10]T. W. Hänsch, Appl. Opt. 11, 895 (1972).
[11]E. U. Condon and G. H. Shortley, *Theory of Atomic Spectra* (Cambridge U.P., London, 1957), Chap. 3.
[12]P. R. Bevington, *Data Reduction and Error Analysis for the Physical Sciences* (McGraw-Hill, New York, 1969), Chap. 11.
[13]S. Y. Chen and M. Takeo, Rev. Mod. Phys. 29, 20 (1957).
[14]T. W. Ducas, M. G. Littman, R. R. Freeman, and D. Kleppner, Phys. Rev. Lett. 35, 366 (1975).
[15]A. Fontijn, Prog. Reac. Kinet. 6, 75 (1971).
[16]P. M. Johnson, J. Chem. Phys. 64, 4143 (1976).
[17]C. M. Lee and K. T. Lu, Phys. Rev. A 8, 1241 (1973).
[18]K. T. Lu and U. Fano, Phys. Rev. A 2, 81 (1970).
[19]K. T. Lu, Phys. Rev. A 4, 579 (1971).

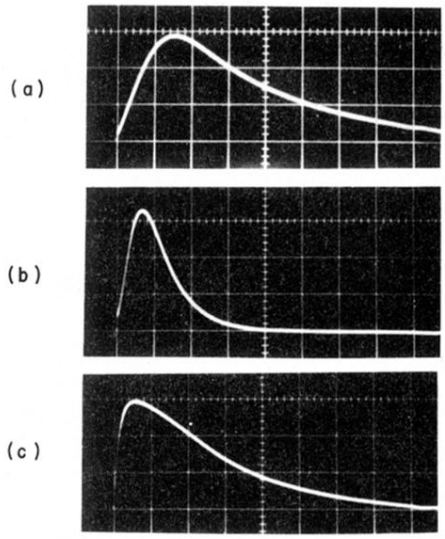


FIG. 3. Typical ionization pulses obtained with parallel plate electrodes and a 100 kΩ load resistor. Vertical: 10 mV/div; horizontal: 0.1 msec/div. (a) Voltage between plates, $V = 0.4$ V, beam focused midway between the plates; (b) $V = 3.78$ V, beam focused as in (a); (c) $V = 0.4$ V, beam focused closer to collecting (negative) electrode.